



Controls on the patterns of topography and erosion rate in a critical orogen

Drew Stolar,^{1,3} Gerard Roe,^{1,2} and Sean Willett^{1,4}

Received 20 November 2006; revised 4 June 2007; accepted 28 June 2007; published 23 October 2007.

[1] We solve for the steady state patterns of erosion rate and topography in a critical wedge to understand the mutual adjustment of tectonics, erosion, and topography in the absence and presence of spatial variations in precipitation rate. We consider steady state systems in which tectonics favors a critical topographic form, assumed to be the mean elevation across the range, and in which surface erosion by rivers and hillslopes operates on a two-dimensional landscape. We find that (1) a nonuniform critical topographic form implies a nonuniform pattern of ridge-valley relief and hence a nonuniform pattern of erosion rate, and (2) when the system is forced by local variations in precipitation rate, maintenance of the critical topographic form requires a local response of rock uplift that greatly dampens changes in topography. We apply these concepts to the western side of the Olympic Mountains of Washington State, where mean elevation, ridge-valley relief, and precipitation rates increase from the coast to the topographic crest of the range. We find that the main control on the erosion rate pattern is the pattern in mean elevation and the amount of precipitation. In contrast, the pattern of precipitation is only a minor control. As a whole, our work demonstrates an approach for developing the theoretical context that is necessary for interpreting spatial associations between patterns in topography, precipitation, and erosion in natural orogens.

Citation: Stolar, D., G. Roe, and S. Willett (2007), Controls on the patterns of topography and erosion rate in a critical orogen, *J. Geophys. Res.*, 112, F04002, doi:10.1029/2006JF000713.

1. Introduction

[2] Over the past two decades, work by a broad community of Earth scientists has led to an increased understanding of the evolution of convergent orogens. The centerpiece is a rich conceptual model, in which mountain building is controlled by tectonic, erosional and climatic processes [Beaumont *et al.*, 1992; Avouac and Burov, 1996; Willett, 1999a; Beaumont *et al.*, 2001]. In this paper, we address one of the principle unknowns in this conceptual model: what are the implications of coupling between tectonics and erosion for the patterns of topography, erosion rate and deformation?

[3] One of the key insights into this question in convergent settings is that topography plays a very important role: body forces from topography influence stresses within the crust and therefore can influence the rate and pattern of deformation. Furthermore, it has been proposed that mean topography in a convergent orogen should evolve toward a specific form, hereafter called a critical topographic form, which represents a balance between internal and boundary

stresses [Davis *et al.*, 1983; Dahlen, 1984]. Perturbations to this topographic form, as might arise from surface erosion, are expected to be compensated by deformation-driven rock uplift, thereby providing a strong connection between the patterns of erosion rate and deformation. Since the notion of critical topography was originally proposed for orogens in which deformation occurs by brittle failure, a number of numerical modeling studies have demonstrated that orogens characterized by other rheologies are also responsive to surface erosion, in the sense that removal of mass from the surface leads to changes in the pattern of deformation [e.g., Beaumont *et al.*, 1992; Willett, 1999a; Beaumont *et al.*, 2001; Godard *et al.*, 2004].

[4] Whereas numerical models have been effective tools for describing the behavior of the coupled system, there is a growing interest in using simpler models based on critical wedge theory to understand how climate and erosion influence an orogen's size and rate of growth [Hilley and Strecker, 2004; Hilley *et al.*, 2004; Whipple and Meade, 2004, 2006; Roe *et al.*, 2006]. However, none of these studies explain how the patterns of erosion and deformation relate to each other: in the first two studies noted above, the pattern of erosion rate was imposed; in the other studies, only the range-average erosion rate was considered. Thus there is a real opportunity to understand how the patterns of erosion and deformation emerge from the mutual interactions between tectonic, erosional, and climatic processes.

[5] In this paper, we present a self-consistent theoretical framework in which to understand the coupling of surface

¹Department of Earth and Space Sciences, University of Washington, Seattle, Washington, USA.

²Quaternary Research Center, University of Washington, Seattle, Washington, USA.

³Now at School of Earth and Space Exploration, Arizona State University, Tempe, Arizona, USA.

⁴Now at Geological Institute, ETH Zurich, Zurich, Switzerland.

erosion and tectonic deformation. We restrict our analysis to a simple tectonic-erosional system, an eroding critical wedge at steady state, and consider only prescribed patterns in precipitation. We begin by using a set of numerical simulations to illustrate the behavior of the coupled system under different patterns of precipitation. The results of these simulations then guide the development of a simpler framework that both reproduces and explains the salient features of the more complicated numerical model. Finally, we use the example of the Olympic Mountains of Washington State to predict the influence of an actual pattern of precipitation on the erosion rate pattern.

2. Numerical Model

2.1. Description of the Numerical Model

[6] We use a tectonic-erosional model that was developed to describe the evolution of accretionary wedge settings [Stolar *et al.*, 2006]. The primary advantage of the model is that it allows us to examine the evolution of a theoretical orogen in which the interactions between tectonics and erosion are not overly prescribed. The tectonic model simulates crustal deformation in response to steady frontal accretion and predicts horizontal and vertical velocities within a two-dimensional, cross-sectional domain (Figure 1) [Willett *et al.*, 1993; Willett, 1999a]. We assume a Coulomb plastic rheology such that the tectonic system behaves like a critical wedge orogen: internal deformation and sliding along the base maintain the form of the upper surface, which is expected to have a constant slope over much of the orogen [e.g., Dahlen, 1984; Wang and Davis, 1996; Willett, 1999b; Stolar *et al.*, 2006]. In later sections, we demonstrate that the results of our work do not rely heavily on the specific topographic form.

[7] We also assume no isostatic compensation. This assumption is appropriate in our study because, as is demonstrated by the numerical modeling results, the across-orogen patterns of minimum, mean and maximum elevation achieve relatively steady forms. Because the across-orogen pattern of topography, and hence crustal loading, is steady, it follows that isostasy would not influence the across-orogen patterns of deformation or erosion.

[8] Surface erosion is simulated in planform with the Cascade surface process model [Braun and Sambridge, 1997], which solves for surface mass transport on an irregular network of nodes. At any given time during orogen evolution, the model landscape is divided into two process regimes: bedrock channels and hillslopes. Hillslopes are stipulated to have a threshold slope, s_c . Within the channel network, the stream power law is used to calculate the erosion rate, e :

$$e = kq^m s^n, \quad (1)$$

where k is a measure of the bedrock erodibility, q is the water discharge, s is the downstream slope, and m and n are related to the physical processes of bedrock erosion [e.g., Whipple and Tucker, 1999; Whipple *et al.*, 2000; Finnegan *et al.*, 2004]. We chose $m = 1/2$ and $n = 1$ (unit stream power) and assume purely detachment-limited conditions; that is, sediment does not influence the incision rate [Sklar and Dietrich, 2001, 2004; Whipple and Tucker, 1999, 2002].

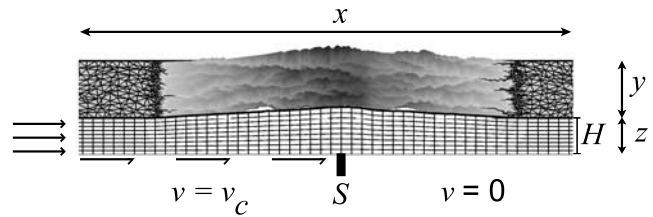


Figure 1. Numerical model with dimensions and boundary conditions. Tectonic model is solved in the vertical plane (mesh is coarsened for display purposes). The surface process model is solved in planform. The surface process model domain has x and y lengths of 1000 and 60 km, respectively, but for display purposes, the entirety of the x dimension is not shown. Height of incoming crust, H , is 10 km. The basal velocity decreases from the convergence velocity ($v_c = 20$ km/Ma) to zero at point S .

[9] Recent theoretical considerations suggest that some of the complexities now recognized to influence bedrock incision, e.g., changes in bedrock channel width and a tools-and-cover effect of sediment, lead to fluvial erosion laws with the same functional form as equation (1). For example, Finnegan *et al.* [2004] suggested that channel width might itself be a power law function of discharge and slope, such that the erosion rate follows equation (1). Also, Whipple and Tucker [2002] and Gasparini *et al.* [2006] have shown that, at topographic steady state, some sediment-dependent erosion laws collapse to equation (1). Thus, with the notable exception of erosion thresholds [e.g., Lavé and Avouac, 2001; Snyder *et al.*, 2003], the functional form of the stream power law appears to be fairly accommodating to geomorphic complexity. The robustness of equation (1) is particularly useful in this study because, as is demonstrated below, the general results do not depend on the specific values of k , m or n . In the discussion section, we will revisit the implications of deviations from the stream power law.

[10] In the numerical model, surface erosion and tectonic deformation are coupled in both directions. The mean elevation across the landscape generated by the surface process model is used as the upper surface of the tectonic model (thick black line in Figure 1). In turn, horizontal and vertical velocities calculated along the upper surface of the tectonic model are used as forcing conditions in the surface process model [e.g., Beaumont *et al.*, 1992]. Thus changes in the landscape are transmitted to the tectonic system and vice versa.

2.2. Numerical Model Results

[11] We investigate the response of the coupled system to two simple patterns of precipitation. We first examine the case of uniform precipitation. This provides a reference for the nonuniform case, which follows, and allows us to address the question of whether uniform precipitation produces a uniform response in rock uplift, deformation and erosion rates. Second, we apply a nonuniform pattern of precipitation that includes a narrow zone, midway up the critical slope of the wedge, in which the precipitation rate is increased by a factor of eight. The precipitation variation is made extreme for illustrative purposes, as this experiment dramatically illustrates the response of the coupled system

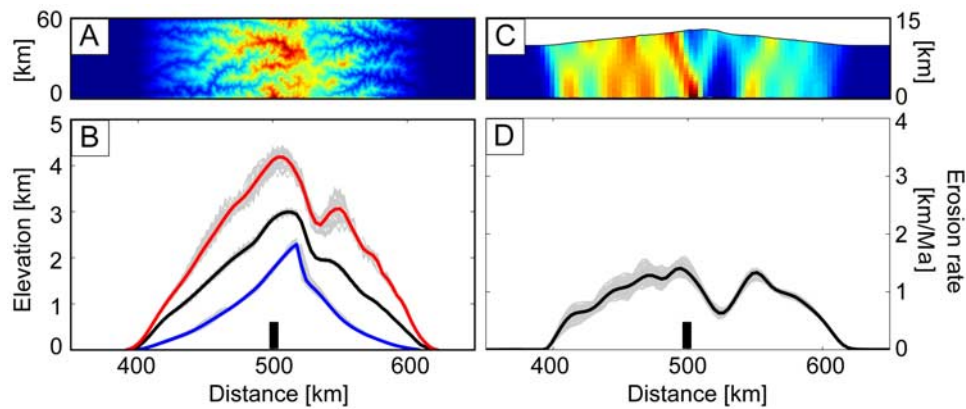


Figure 2. Numerical model results from uniform precipitation scenario. (a) Planform topography at $t = 10$ Ma, with warmer colors representing higher elevations. (b) Minimum, mean, and maximum elevation profiles across the orogen (thick lines). These have been averaged over 4 Ma during which the long-wavelength topography is at steady state. Seventeen profiles from 0.25 Ma intervals during this same period are shown in gray. The detachment point S of the tectonic model is denoted by the black bar. (c) The xx component of the strain rate tensor at $t = 10$ Ma, with warmer colors representing higher strain rates (i.e., higher spatial gradients in the horizontal velocity). (d) Time- and space-averaged erosion rate profile as defined in Figure 2b, with 17 profiles at 0.25 Ma intervals shown in gray. Parameter values are $m = 1/2$, $n = 1$, $k = 2 \times 10^{-6} \text{ m}^{-1/2} \text{ yr}^{-1/2}$, and $s_c = 30^\circ$, and the precipitation rate is 1 m/yr.

to nonuniform precipitation; more realistic precipitation patterns are considered in section 7.

2.2.1. Uniform Precipitation

[12] The results of the uniform precipitation simulation are presented in Figure 2. The simulated orogen begins as a nearly flat landscape with small random perturbations and grows until it reaches a steady size. Because horizontal rock velocities are nonzero over the entire orogen, planform topography never achieves a perfect steady state: a snapshot of the planform topography is shown in Figure 2a. However, other important characteristics of the orogen do attain steady state: the steady state minimum, mean and maximum elevation across the range are shown in Figure 2b (thick lines); the xx component of the steady state strain rate tensor is shown in Figure 2c; the steady state erosion rate across the range is shown in Figure 2d (thick black line). Note that, at steady state, the erosion rate, e , and the velocity of rock at the surface are related by: $e = u - v \, dz/dx$, where dz/dx is the slope of the mean topography and u and v are the vertical and horizontal rock velocities, respectively. In the simulations presented here, the mean topographic slope is small, such that the pattern of erosion rate mostly reflects variations in the vertical rock velocity [Stolar *et al.*, 2006].

[13] The results in Figure 2 reveal two important scales of variation. At the largest scale, the patterns of topography, deformation and erosion rate vary in the same way: they increase toward the center of the range. Mean elevation increases toward the main divide, with a slope (1.5°) that is consistent with the internal and basal friction angles (20° and 3° , respectively) assumed in the tectonic model [Dahlen, 1984]. Deformation rates also increase away from the pro- and retro-wedge toes. Erosion rates are near zero at the pro- and retro-wedge toes and increase to maxima close to the main divide. We also note that ridge-valley relief, which we define as the difference between the maximum and minimum elevation, follows a very similar trend.

[14] There is also variation at the scale of the crustal thickness. This is due to localization of strain within shear zones, which are oriented at roughly 45° from horizontal and occur as conjugate pairs (Figure 2c). Focusing of deformation within these zones is reflected by local maxima in the mean elevation and erosion rate (Figures 2b and 2d). We return to these features in the discussion.

[15] The key result from this simulation is that significant spatial variability in deformation, erosion and topography can arise even with uniform precipitation; we explore the physical reasons for this in a later section.

2.2.2. Nonuniform Precipitation

[16] To illustrate the response of the coupled model to nonuniform precipitation, we impose an eightfold increase in precipitation rate within a narrow zone oriented parallel to the strike of the orogen. As noted above, this box car pattern is not intended to be realistic but is useful for illustrative purposes.

[17] The results of the nonuniform precipitation simulation are shown in Figure 3. Figures 3a and 3b show that localization of precipitation produces only small changes in the topography. Relative to the uniform precipitation scenario, orogen width decreases by 10%. This is expected since the mean precipitation rate and thus the mean erosion rate over the orogen have increased [e.g., Hilley and Strecker, 2004; Whipple and Meade, 2004; Roe *et al.*, 2006]. Within the zone of increased precipitation, the ridge-valley relief decreases by 3%. The change in relief is remarkably small considering that, relative to the uniform precipitation scenario, the local precipitation rate has increased by 700%.

[18] The local responses of erosion rate and deformation are much more dramatic. Whereas the mean erosion rate over the orogen increases by 15% as a consequence of the decrease in the orogen width, the erosion rate within the zone of increased precipitation increases by 115%

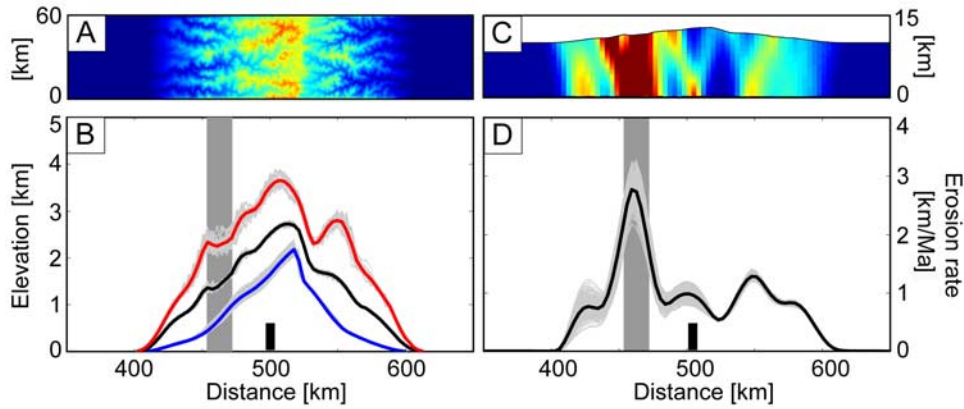


Figure 3. Numerical model results from the nonuniform precipitation scenario. See caption of Figure 2 for more details. (a) Planform topography, (b) elevation profiles, (c) strain rate, and (d) erosion rate profiles. Gray bar represents the region in which the precipitation rate is eight times that of the background rate. Other parameter values are the same as in Figure 2.

(Figure 3d). Deformation rates are also very high in this region (Figure 3c), and the xx component of the strain rate tensor reveals that horizontal rock velocities decrease rather sharply across the region of increased precipitation. Thus there is a striking difference between the topographic and deformation responses: localized precipitation leads to a very weak topographic response and much stronger erosion and deformation responses.

[19] Taking the key results of the numerical simulations as motivation for further investigation, the target for the remainder of this paper is to understand the following two questions in the simplest manner possible: (1) Why does uniform precipitation result in nonuniform deformation and nonuniform erosion rate? and (2) why are the topographic and deformation responses to nonuniform precipitation so different? Eventually, we show that aspects of a two-dimensional landscape are crucial for understanding the answers to both questions. To begin with, however, we first assume that the inverse is true. That is, a one-dimensional landscape is sufficient. By showing that the predictions of a one-dimensional landscape are vastly different from the numerical model results, we make an initial argument for the importance of a two-dimensional landscape, which is then supported in later sections.

3. One-Dimensional Model

[20] The tectonic and erosional components of the coupled system can both be reduced to one-dimensional representations. We assume a critical wedge with a surface taper angle, α , and represent the landscape as a single river profile [e.g., *Beaumont et al.*, 1996; *Willett*, 1999a; *Hilley and Strecker*, 2004; *Hilley et al.*, 2004]. Therefore, in this model, the river has a constant slope of $\tan(\alpha)$. Letting x be the distance from the divide, the water discharge, q , in the case of uniform precipitation is

$$q = pk_a x^h, \quad (2)$$

where p is the precipitation rate, k_a is a constant and h is the inverse of the Hack exponent. Assuming that the river

erodes according to the stream power law (equation (1)), the erosion rate is simply

$$e = (kk_a^m p^m \tan^n \alpha) x^{hm}. \quad (3)$$

Because the exponent on distance, hm , is positive, the one-dimensional model predicts that the erosion rate is zero at the divide and increases with distance from the divide. This is essentially the opposite of the numerical model result (Figure 2d).

[21] If precipitation rates are increased within a zone located somewhere between the divide and the wedge toe, the erosion rate will increase wherever the water discharge is higher, i.e., both within and downstream of the precipitation increase. Again, this prediction does not agree with the numerical model results (Figure 3d), in which the erosion rate response is localized about the zone of increased precipitation.

[22] Despite the difference in complexity, the tectonic components of the one-dimensional and numerical models obey similar, linear critical topographic forms. The crucial difference between the two models is that, in the numerical model, ridge-valley relief is allowed to exist. In the next section, we examine the implications of ridge-valley relief for the pattern of erosion rate.

4. Trellis Model

[23] We introduce the effect of ridges and valleys by considering a very simple surface process model (Figure 4a). The drainage pattern is a symmetric trellis network. Each tributary drains into the main channel and is connected to the ridge by a threshold hillslope. This model is nearly identical to that of *Lavé* [2005] and *Godard et al.* [2004], with the only significant difference being that the angle between the tributaries and the main channel is 90° , whereas these studies assumed an angle of 40° . As explained below, the principal advantage of a perpendicular drainage network is the very simple connection between ridge-valley relief and local rock uplift and erosion rates: at a given point along the main channel, the rock uplift rate that influences the

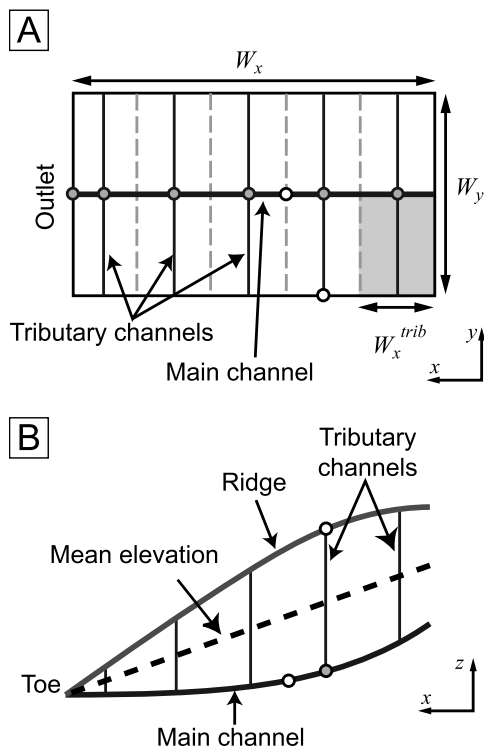


Figure 4. Trellis model. (a) Planform view of the trellis model. Main and tributary channels are shown by solid lines, and tributary boundaries are shown by dashed lines. Main channel elevation is defined at tributary junctions (gray circles) and is zero at the outlet. Ridge profile elevation is defined at the upper end of each tributary. (b) Cross-section view. Mean elevation profile (black dashed line) is the average of the main channel and ridge elevations. Ridge-valley relief is the difference between the main channel and ridge profiles. Circles with black borders mark the three points used for the perturbation analysis in section 6.

main channel slope is the same rock uplift rate that influences the ridge-valley relief. As a result, this surface process model is more conducive to analysis.

[24] The critical wedge model requires that the average cross-strike elevation has a constant slope in the x direction (Figure 4b). Note that this definition of the mean elevation is an average of two points, the ridge and channel elevations, rather than the integrated average of the tributary profile. We assume that rock velocities are purely vertical and that a pointwise topographic steady state exists throughout the model domain. Because rock uplift rate has a more intuitive connection with ridge-valley relief, we switch terminology and use rock uplift rate instead of erosion rate for the remainder of this section and for the following section. Finally, rock uplift rates and precipitation rates are uniform in the y direction and within each tributary basin, and the slope of the main channel is constant between tributary boundaries.

[25] For a critical wedge with a surface taper angle of α , the mean elevation, \bar{z} , is equal to $x\tan\alpha$, where x is the distance from the toe of the wedge (Figure 4). The mean

elevation at the i th tributary junction, \bar{z}_i , must also be equal to the sum of the main channel elevation, z_i , and one half of the ridge-valley relief, r_i , within the tributary basin:

$$\bar{z}_i = z_i + r_i/2. \quad (4)$$

For a landscape with N pairs of matching tributary basins, equation (4) must hold at each main channel-tributary junction; that is, equation (4) is a closed system of equations that can be used to solve for rock uplift rate pattern.

[26] In Appendix A, we derive expressions for the main channel elevation (equation (A2)) and ridge-valley relief (equation (A4)) in terms of specified parameters (e.g., k , p_i , q_i) and unknown rock uplift rates, u_i . For a specified accretionary flux, precipitation rate pattern and drainage network, we can solve for the rock uplift rates using the Newton-Raphson method. We use the same parameters (e.g., taper angle and accretionary flux) as in the numerical model and contrast the same two cases of uniform and nonuniform precipitation. For simplicity, we consider only one side of a symmetric wedge. The extension to an asymmetric wedge is straightforward, following *Whipple and Meade* [2006].

4.1. Uniform Precipitation Results

[27] Elevation and rock uplift rate profiles for the uniform precipitation rate scenario are shown in Figure 5. They are very similar to the results of section 2.2.1 (Figures 2b and 2d). Ridge-valley relief and rock uplift rate are near zero at the toe and increase toward the main divide. Note that the maxima in rock uplift rate and ridge-valley relief are coincident and occur where the slope of the main channel matches the taper angle.

4.2. Nonuniform Precipitation Results

[28] Elevation and rock uplift rate profiles for the nonuniform precipitation scenario are shown in Figure 6. As with the case of nonuniform precipitation, the results are consistent with the results of section 2.2.2 (Figure 3). The model in Figure 6 has more total precipitation than the previous model (Figure 5), and therefore the wedge is narrower at steady state. Within the zone of increased precipitation, the main channel slope is higher than in regions upstream and downstream, as was the case in Figure 2b. Relative to the uniform precipitation scenario, the ridge-valley relief in the zone of increased precipitation decreases by 12%, whereas the rock uplift rate increases by 160%.

[29] The numerical model and the simpler trellis model exhibit the same fundamental behavior: uniform precipitation results in nonuniform deformation and erosion; nonuniform precipitation results in a relatively strong erosion and rock uplift response and a very weak topographic response. As we show in the next two sections, these results can be understood by examining the trellis model in greater detail.

5. Understanding the Response to Uniform Precipitation

[30] In this section, we explain the response to uniform precipitation by exploiting the relationship between ridge-

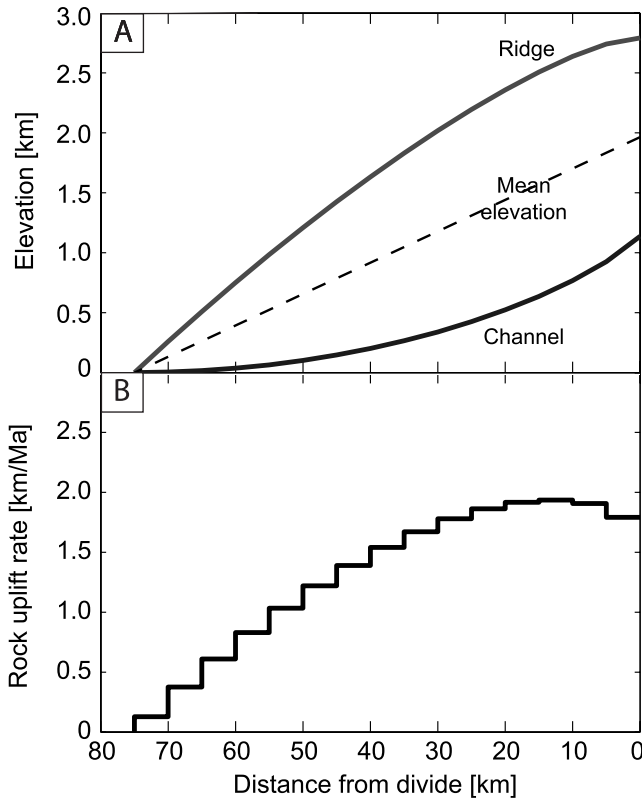


Figure 5. Results from the trellis model for uniform precipitation. (a) Channel, ridge, and mean elevation profiles for a one-sided wedge under uniform precipitation. Parameter values are $m = 1/2$, $n = 1$, $k = 3.47 \times 10^{-6} \text{ m}^{-1/2} \text{ yr}^{-1/2}$, $s_c = 45^\circ$, $p = 1 \text{ m/yr}$, a taper angle of 1.5° , and an accretionary flux of $100 \text{ km}^2/\text{Ma}$. (b) Rock uplift rate profile for the same wedge.

valley relief and rock uplift rate. The stream power law (equation (1)) predicts a positive dependence between channel slope and erosion rate, regardless of the state of topography ($2/3 \leq n \leq 2$ [Whipple and Tucker, 1999]). At topographic steady state, equation (1) can be rearranged to express the channel slope in terms of the vertical rock velocity at the surface, u :

$$s = \left(\frac{u}{k}\right)^{1/n} q^{-m/n}. \quad (5)$$

Thus a higher rock uplift rate results in a higher tributary channel slope, which integrates to yield an increased ridge-valley relief [e.g., Whipple and Tucker, 1999]. Note that this relationship breaks down when the “tributary” consists only of a threshold hillslope. This case arises when rock uplift rates outpace the erosive potential of the fluvial network; however, we do not consider this case any further in this paper. The important aspect of the positive dependence, or mapping, between rock uplift rate and ridge-valley relief is that, if one demonstrates the existence of bounds on the ridge-valley relief, one also demonstrates the existence of bounds on the rock uplift rate.

[31] The simple geometric constraint of equation (4) makes it possible to derive minimum and maximum bounds

on ridge-valley relief (also see Figure 4b). For a critical wedge with mean elevation, \bar{z} , the minimum possible ridge-valley relief is zero (i.e., $z = \bar{z}$), and the maximum is equal to two times the mean elevation (i.e., $z = 0$). Importantly, both bounds go to zero at the toe. It follows that the actual ridge-valley relief must be zero at the toe and increase away from it. In the trellis model, this relief is maintained by tributaries of constant width that experience only one rock uplift rate. Therefore, if relief must increase away from the toe, rock uplift rates must also increase away from the toe. Thus, within this framework, the patterns of ridge-valley relief, rock uplift and erosion rate are inherently nonuniform.

[32] Similar reasoning explains the coincidence of the maxima in rock uplift rate and ridge-valley relief. By definition, the maximum in relief should occur where the derivative of relief with respect to x , $\Delta r/\Delta x$, equals zero. Taking the difference of equation (4) and rearranging yields

$$\frac{\Delta r_i}{\Delta x} = 2 \left(\frac{\Delta \bar{z}_i}{\Delta x} - \frac{\Delta z_i}{\Delta x} \right), \quad (6)$$

where the first term on the right-hand side is simply the taper angle of the wedge. The maximum in relief occurs where the right-hand side of equation (6) is zero, i.e., where the main channel slope matches the taper angle (Figure 5a). Given the positive relationship between ridge-valley relief

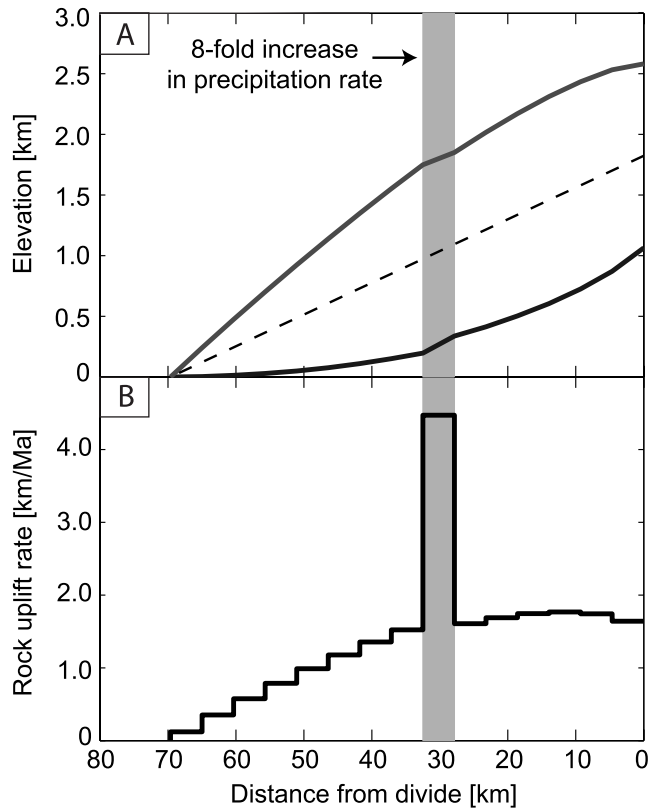


Figure 6. Results from the trellis model for nonuniform precipitation. (a) Main channel, ridge, and mean elevation profiles for an eightfold increase in precipitation rate midway between the divide and toe. (b) Rock uplift rate profile for the same wedge. Parameter values are the same as in Figure 5. See caption of Figure 5 for more information.

and rock uplift rate, it follows that the rock uplift rate has a maximum at the same location (Figure 5b).

[33] The results of this analysis emphasize the importance of the relationship between ridge-valley relief and rock uplift rate. Nonuniform bounds on relief imply a nonuniform rock uplift rate pattern. This association should be fairly general. It requires only (1) a critical topographic form that increases from the toe and (2) a positive relief–rock uplift relationship. Implications for natural systems, where these assumptions might not strictly hold, are considered in the discussion.

6. Understanding the Response to Nonuniform Precipitation

[34] With further simplification of the landscape, we can determine the responses of rock uplift rate and ridge-valley relief to a local change in precipitation. We reduce the landscape to three points (circled points in Figure 4b): a point on the ridge, a point below at the main channel-tributary junction, and a fixed point farther downstream on the main channel. We consider a scenario in which the precipitation rate is increased within the tributary basin by an amount Δp . The increase in precipitation rate is represented in the main channel by an increase in water discharge of Δq . It is important to note that the fractional increase in the main channel discharge, $\Delta q/q$, is less than or equal to the fractional change in precipitation rate, $\Delta p/p$, because the main channel discharge integrates over an area larger than an individual tributary basin.

[35] The changes in erosive potential within the tributary basin and along the main channel generate a fractional change in the rock uplift rate, $\Delta u/u$, which in turn influences both the main channel elevation and the ridge-valley relief. In Appendix B, we derive expressions for the responses of the main channel elevation, Δz , and the ridge-valley relief, Δr :

$$\Delta z = \underset{i}{\gamma_z} \left(\underset{ii}{\frac{\Delta u}{u}} - m \frac{\Delta q}{q} \right) \quad (7)$$

and

$$\Delta r = \gamma_r \left(\underset{iii}{\frac{\Delta u}{u}} - m \frac{\Delta p}{p} \right). \quad (8)$$

The responses of main channel elevation and ridge-valley relief can be expressed as straightforward functions of the difference between the tectonic and erosional forcing (terms *ii* and *iv*), multiplied by a sensitivity factor (terms *i* and *iii*). The sensitivity factor γ_z is proportional to the elevation gain of the main channel over one half of a tributary:

$$\gamma_z = \frac{1}{n} s \frac{W_x^{trib}}{2}, \quad (9)$$

where s is the unperturbed main channel slope and W_x^{trib} is the across-strike width of the tributary basin. The sensitivity

factor γ_r is proportional to the fluvial relief, r_f , of the tributary (equation (B10)):

$$\gamma_r = \frac{1}{n} r_f. \quad (10)$$

Because the elevation gained on the main channel is typically small relative to the fluvial relief on the tributary [e.g., Whipple *et al.*, 1999], γ_r should be much greater than γ_z (term *iii* \gg term *i*). In other words, we expect that the ridge-valley relief is much more sensitive to differences between tectonic and erosional forcing than is the main channel elevation.

[36] For an increase in erosive potential, the tendency of both the main channel elevation and ridge-valley is to lower. However, maintenance of the critical topographic form requires that $\Delta \bar{z} = 0$: hence changes in the main channel elevation and ridge-valley relief must be of opposite sign. Taking the difference of equation (4) and setting $\Delta \bar{z}$ equal to zero yields the exact relationship

$$\Delta z = -\Delta r/2. \quad (11)$$

Equation (11) requires that the rock uplift rate must change for a balance to be struck between the requirement of a critical taper and the changes in erosive potential. Given that the fractional change in the main channel discharge ($\Delta q/q$) is less than or equal to the fractional increase in precipitation within the tributary ($\Delta p/p$), the rock uplift response can be simplified to

$$m \frac{\Delta q}{q} \leq \frac{\Delta u}{u} \leq m \frac{\Delta p}{p}. \quad (12)$$

Thus the fractional change in rock uplift rate is bounded by m times the fractional changes in the main channel discharge and the tributary precipitation rate. The outcome of the first inequality in equation (12) is that the slope and elevation of the main channel must increase ($\Delta z > 0$). The outcome of the second inequality is that the ridge-valley relief must decrease ($\Delta r < 0$). Both of these predictions are observed in the numerical and trellis model results (see Figures 3a, 3b, 6a and 6b).

[37] Equations (7) through (11) are also strong constraints on the magnitudes of the ridge-valley relief and rock uplift rate responses. Referring to the labels given to the different terms in equations (7) and (8), equation (11) requires that (*i*) \times (*ii*) and (*iii*) \times (*iv*) differ by only a factor of two. However, as noted above, there is good reason to expect that (*iii*) \gg (*i*). The only way these two things can be true is if (*iv*) \ll (*ii*). Therefore it must be true that $\Delta u/u$ is much closer in value to $m\Delta p/p$ than to $m\Delta q/q$. Thus a local variation in precipitation is expected to be accommodated by a relatively large rock uplift response and a small relief response.

[38] The final result of this analysis concerns the scale of the rock uplift rate response. In the trellis model, it is almost completely limited to the extent of the zone of increased precipitation. However, within the main channel, the relative increase in discharge is roughly the same downstream as it is within the zone of increased precipitation; that is, the erosional forcing of the main channel is about the same.

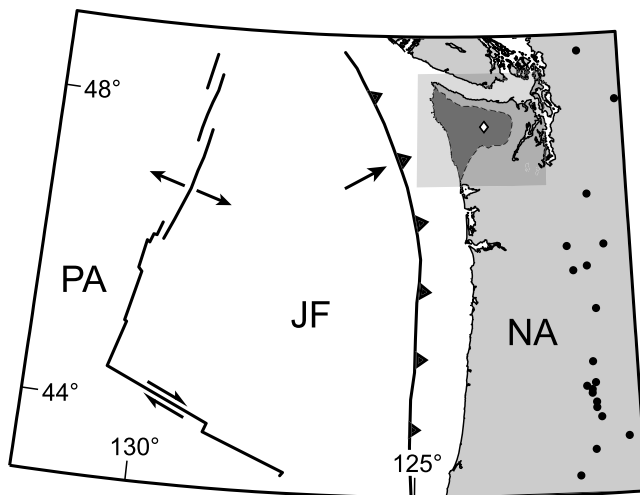


Figure 7. Cascadia margin. The Olympic peninsula is bounded by the semitransparent box. The Olympic accretionary wedge is shown in dark gray and abuts the Crescent terrane to the north, east, and south. The white diamond denotes the location of Mount Olympus. Small black circles mark the location of Holocene volcanoes, which delineate the Cascade volcanic arc. NA, North American plate; PA, Pacific plate; JF, Juan de Fuca plate. Orientations of the relative plate motions are shown for the PA-JF and JF-NA boundaries.

However, the tributary within the zone of increased precipitation experiences eight times more precipitation than does the downstream tributary basin; that is, the erosional forcing on the tributary is very different. The result is that the rock uplift rate increases dramatically within the zone of increased precipitation and is barely changed outside of that zone. Thus, in this framework, tributaries play a crucial role in determining both the length scale and magnitude of the rock uplift rate response. We address the geologic plausibility of this result in the discussion section.

[39] Up to this point, the nonuniform pattern of precipitation employed in this paper has been useful for demonstrating the fundamental difference between the topographic and erosion rate responses to spatial variations in precipitation. However, it is important to understand the effects of realistic patterns of precipitation on realistic drainage networks. In the following section, we quantify the influence of a twofold variation in precipitation on the erosion rate pattern on the western side of the Olympic Mountains of Washington State.

7. Application to the Olympic Mountains

7.1. Setting

[40] The Olympic Mountains are located along the Juan de Fuca–North America plate boundary in the northwestern corner of the continuous United States (Figure 7) and are the result of at least thirty million years of accumulation and accretion of sediments onto the North American plate [Tabor and Cady, 1978]. The topography of the range represents a significant orographic barrier to moisture-laden air coming from the Pacific Ocean and results in a strong rain shadow, with precipitation rates doubling from the

western coast to the topographic crest, Mount Olympus, and then decreasing sharply to the east [Anders *et al.*, 2007]. The high topographic relief and high precipitation rates are associated with fairly rapid erosion (~ 1 km/Ma in the interior of the range) that, sustained over geologic time-scales, has led to a significant amount of exhumation (10–15 km in the interior of the range) [Brandon *et al.*, 1998]. Because of this combination of factors, the Olympic Mountains are well suited as a setting for investigations into the roles of tectonics, erosion and climate in orogen evolution [e.g., Brandon *et al.*, 1998; Willett, 1999a; Montgomery and Greenberg, 2000; Pazzaglia and Brandon, 2001; Batt *et al.*, 2001]. Furthermore, because many of the assumptions underlying our analyses are reasonably met there, the Olympic Mountains are a particularly apt setting for this study. In the next few paragraphs, we provide supporting evidence—and caveats—about four key assumptions that are necessary for further analysis of the Olympic Mountains: two-dimensional, plane strain deformation; steady state topography; fluvially dominated erosion; and a steady precipitation pattern.

[41] In the vicinity of the Olympic Peninsula, convergence between the Juan de Fuca plate and the Cascadia forearc, which extends from northern California through the Oregon Coast Range and the Olympic Mountains, occurs at a velocity of 30–35 km/Ma and an azimuth of approximately 55° – 60° E [Miller *et al.*, 2001; Wang *et al.*, 2003]. Submarine features of the margin, such as the deformation front and the continental shelf, have azimuths of about 160° and are nearly orthogonal to the convergence direction, indicating that accretion and deformation occur primarily in the across-strike plane. The broad domal topography and radial drainage network of the Olympic Mountains (Figure 8a) seem at odds with this scenario, and indeed, there are suggestions from paleomagnetic and geodetic studies that a sizable amount of along-strike convergence might be accommodated across the range [e.g., Wells, 1990; McCaffrey *et al.*, 2000; Miller *et al.*, 2001]. However, in this analysis, we adopt the perspective of Brandon and Calderwood [1990] that the domal form of the range is the result of the bend in the subducting Juan de Fuca slab (Figure 7), not along-strike convergence. We focus on the western flank of the range, where the relevant stresses due to topography and to coupling with the subducting slab are aligned with the general orientation of major drainage networks and hence the major direction of surface mass transport.

[42] Both geomorphic and thermochronometric studies have shown that the pattern of erosion in the Olympic Mountains has remained relatively steady since 10–14 Ma [e.g., Brandon *et al.*, 1998; Pazzaglia and Brandon, 2001; Batt *et al.*, 2001; D. B. Stolar *et al.*, Using low-temperature thermochronometers to determine the long-term erosion rate pattern in the Olympic Mountains of Washington State, manuscript in preparation, 2007, hereinafter referred to as Stolar *et al.*, manuscript in preparation, 2007]. The more straightforward implication of these findings is that there is a persistent, if approximate, balance between rock uplift and erosion in the range; that is, topography is in a large-scale steady state. The more subtle implication is that Quaternary glaciation has not had a measurable influence on long-term erosion rates, at least as inferred from low-temperature

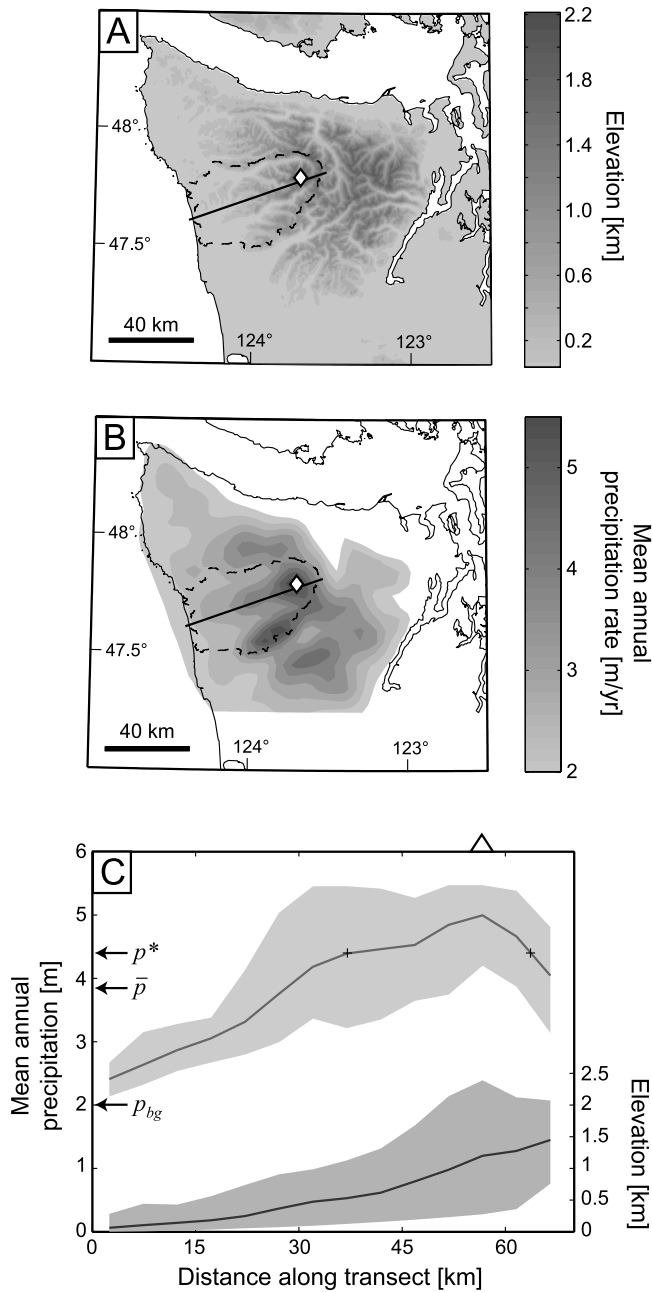


Figure 8. Olympic peninsula. (a) The 100-m digital elevation model (DEM) of the Olympic peninsula. The analysis domain is outlined by the dashed line. Transect is across the western side of Mount Olympus. (b) Contour map of mean annual precipitation as predicted by MM5, a mesoscale forecast model, for the period of 1999–2004 [Anders *et al.*, 2007]. (c) Minimum, mean, and maximum profiles of elevation and mean precipitation rate across the analysis domain. Here \bar{p} is the mean precipitation rate over the entire analysis domain (3.86 m/yr), p_{bg} is an estimate of the precipitation rate in the absence of orographically enhanced precipitation, and p^* is the effective mean precipitation rate (4.3–4.45 m/yr for m and n values used here; see text for further explanation). Pluses mark the locations along the transect where the mean precipitation profile (bold gray line) is equal to p^* . Triangle denotes the location of Mount Olympus.

thermochronometry; that is, erosion is dominated by fluvial and hillslope processes. Studies of the topography of the Olympic Mountains provide both supporting and conflicting evidence for the latter implication. Montgomery [2002] argued that the most significant modification to the landscape by Quaternary glaciation was a widening, rather than a deepening, of major valleys. However, Montgomery and Greenberg [2000] estimated that isostatic rebound due to valley deepening by glacial erosion during the Quaternary could account for up to 30% of the elevation of Mount Olympus (2427 m). Though we recognize that the assumptions of topographic steady state and fluvially dominated erosion are unlikely to hold on a point-by-point basis, they seem appropriate for this analysis because, as demonstrated below, the general results depend on the large-scale trends, not the details, in the topography of the Olympic Mountains.

[43] Estimates of the modern-day pattern of precipitation (Figure 8b) come from a mesoscale forecast model, MM5, from which Anders *et al.* [2007] analyzed daily precipitation rates on 4.5 km grid for the time period of 1999–2004. In general, the variation in precipitation from the wetter, western side to the drier, eastern side is typical of orographic precipitation in coastal midlatitude settings [e.g., Roe, 2005]. Anders *et al.* [2007] found reasonable agreement between the forecast predictions of precipitation and measurements from an high spatial resolution gauging network on a ridge on the western side of the range. Importantly, they also found that the spatial variations in precipitation during large storm events, which occurred under a wide range of climatological conditions, closely mimicked the multiyear precipitation pattern shown in Figure 8b. From this, Anders *et al.* [2007] inferred that the precipitation pattern is a relatively robust feature of the topography and midlatitude setting of the Olympic Mountains, i.e., that Figure 8b is a reasonable estimate of the precipitation pattern over geologically relevant timescales.

[44] In the remainder of this section, we consider the patterns of topography and precipitation on the western side of the range. To describe these patterns in a way similar to previous sections, we delimit an analysis domain that encompasses the Hoh, Clearwater and Queets drainage basins, as well as two small basins near the coast (Figure 8a). Within the analysis domain, we construct a set of 5-km-wide swaths that are oriented parallel to the plate boundary and calculate the minimum, mean and maximum values of elevation and precipitation within each swath. These values are then projected onto a transect that runs from the western coast through Mount Olympus (Figure 8c).

[45] Mean precipitation across the analysis domain increases from ~ 2.5 m/yr at the coast to ~ 5 m/yr at Mount Olympus. Mean elevation increases gradually away from the coast to the divide with a slope of 1° . Ridge-valley relief, which we define as the difference between the maximum and minimum elevation profiles, also increases away from the coast and reaches a maximum at Mount Olympus.

[46] These observations allow for a preliminary prediction for the pattern of erosion rate on the western side of the range. Given the proposed relationship between erosion rate and ridge-valley relief for the case of uniform precipitation, the increase in ridge-valley relief toward Mount Olympus suggests, by association, that erosion rates also increase

toward Mount Olympus [e.g., *Montgomery and Brandon, 2002*]. Furthermore, the doubling of precipitation rates across the western side of the range should amplify the erosion rates near Mount Olympus. Thus there are two factors, albeit interdependent, that favor an increase in erosion rate toward Mount Olympus. However, can we determine how much of an influence the precipitation pattern has on the predicted erosion rate pattern?

7.2. Methodology

[47] We address this question with a methodology similar to that used in the trellis model. In outline, we assume that the observed mean elevation profile (Figure 8c) is the critical topographic form of the orogen and, using both the observed pattern of precipitation and several uniform patterns of precipitation, we solve for the erosion rate patterns that produce the observed mean elevation profile. Fitting the mean elevation profile does not guarantee that the predicted ridge-valley relief matches the observed ridge-valley relief, so we search for the combinations of m and n that best explain the ridge-valley relief. Then, for several acceptable combinations of m and n , we compare the predicted erosion rate patterns to determine the influence of the nonuniform pattern of precipitation. Finally, we compare the predicted erosion rate patterns to two inferred erosion rate patterns.

[48] In detail, we assume that the erosion rate pattern along the transect is a step function composed of 5-km-wide segments. Note that the results of the model do not depend much on the width of the segments. Within each segment, the erosion rate is constant. The mean erosion rate along the transect is assumed to be 0.5 km/Ma, which is representative of erosion rates on the western side of the range derived from river incision rates and low-temperature thermochronometer data [e.g., *Brandon et al., 1998; Pazzaglia and Brandon, 2001; Batt et al., 2001*]. We extract the drainage network from the filled 100-m digital elevation model (DEM) and, for a given pattern of precipitation, calculate the mean annual water discharge at every point. Given the relatively homogeneous lithology of the accreted rocks that comprise the western side of the range [*Tabor and Cady, 1978*], we assume that the bedrock erodibility, k , is constant over the entire domain. In the discussion section, we consider how spatial variations in bedrock erodibility might influence the erosion rate pattern.

[49] We assume that all hillslopes in the model are characterized by a gradient, s_h , that is constant over the length of the hillslope, much like was assumed in previous sections. In the Olympic Mountains, the mean local slope averaged over many square kilometers varies significantly, from 10° near the western coast to 30° near Mount Olympus [*Montgomery, 2001*]. We account for this variation by assuming that s_h is the mean hillslope gradient within each swath as calculated from the 100-m DEM. The local slope of any point i in the j th swath is then given by

$$s_i = \min\left(\left(\frac{e_j}{k}\right)^{\frac{1}{n}} q_i^{-\frac{m}{n}}, s_{hj}\right). \quad (13)$$

The elevation within the analysis domain is calculated by integrating equation (13) from each drainage basin outlet, which is assumed to be fixed at sea level. For a predicted

planform topography, the mean elevation within each swath can be calculated and compared to the observed mean elevation (Figure 8c). As in the trellis model, we use the Newton-Raphson method to solve for the erosion rate profile that agrees with the observed mean elevation profile.

7.3. Results

[50] We first present results using the observed pattern of precipitation. For a range of m and n values ($1/4 \leq m \leq 1$, $1/2 \leq n \leq 2$), we solve for the erosion rate pattern and compute the root-mean-square (RMS) misfit between the observed and predicted ridge-valley relief. Because the units of k are dependent on m , the value of k is adjusted for each combination of m and n such that the mean erosion rate across the transect is always 0.5 km/Ma.

[51] A contour plot of the RMS misfit is shown in Figure 9a, with lighter colors representing a closer match to the observed ridge-valley relief. The minimum misfits are ~ 120 m, and the mean ridge-valley relief is 1050 m (Figure 9b). The relatively small misfits suggest a reasonable consistency between the topography of the Olympic Mountains and a steady state landscape in which erosion is dominated by fluvial and hillslope processes [e.g., *Pazzaglia and Brandon, 2001*].

[52] Misfit in relief is almost entirely dependent on the ratio of m and n , not the individual values. The best fit value of m/n is ~ 0.5 . An equivalent exercise using a different definition of relief (relief is equal to the standard deviation of elevation within each swath) yields a best fit m/n value of ~ 0.6 . The observed ridge-valley relief and the relief predicted for several combinations of m and n are shown in Figure 9b. Note that all of the predicted patterns of relief in Figure 9b are from predicted landscapes whose mean elevation profile is identical to the observed profile. Thus there is a strong suggestion that m/n values in the vicinity of 0.5 can describe both the mean topography and the planform topography of the western side of the Olympic Mountains.

[53] Next, we calculate the erosion rate patterns resulting from the observed pattern of precipitation and three uniform patterns of precipitation. Predictions from the different precipitation scenarios allow us to focus on the influence of spatial variations in precipitation on spatial variations in erosion rate, i.e., to connect our analysis of the Olympic Mountains to the results of the two previous sections. For uniform precipitation patterns, we consider a low background precipitation rate ($p_{bg} = 2$ m/yr), which is a rough estimate of the precipitation rate in the absence of an orographic effect (Figure 8b), the observed mean precipitation rate ($\bar{p} = 3.86$ m/yr), and the effective mean precipitation rate ($p^* = 4.3\text{--}4.45$ m/yr depending on the values of m and n). The distinction between the observed and effective mean precipitation rates is necessary because, in our model, the calculation using the observed mean precipitation rate yields a mean erosion rate that is lower than 0.5 km/Ma ($\bar{e} = 0.46\text{--}0.48$ km/Ma depending on the values of m and n). This is due to an interesting feature of the precipitation pattern in the Olympic Mountains: precipitation rates on the ridges are typically higher than those in the valleys (Figure 8b) [*Anders et al., 2007*]. Because fluvial relief is more sensitive to the precipitation rate close to the divide than near the outlet [*Roe et al., 2003*], the effective mean

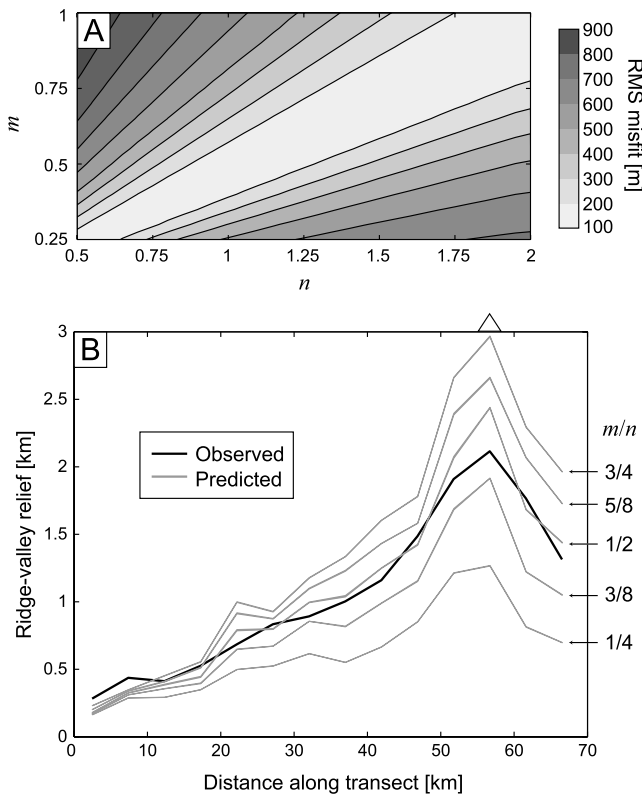


Figure 9. Comparison of predicted and observed topography. (a) RMS misfit of the predicted ridge-valley relief as a function of the fluvial erosion law parameters m and n (equation (1)). Lighter shading represents lower misfit. (b) Observed and predicted patterns of ridge-valley relief for different values of m/n . Small variations in the width of each predicted curve (in gray) reflect the variations due to assuming different values of n ($2/3$, 1 , and $19/16$). Triangle denotes the location of Mount Olympus.

Figure 10. Predicted erosion rate patterns for the observed pattern of precipitation (black lines) and three uniform precipitation rates: a representative background precipitation rate (p_{bg} , black dotted lines), the observed mean precipitation rate (\bar{p} , dashed dark gray lines), and the effective mean precipitation rate (p^* ; solid gray lines) for three different fluvial erosion laws: the unit shear stress model ($m = 1/3, n = 2/3$), the unit stream power model ($m = 1/2, n = 1$), and the model of Finnegan *et al.* [2004] ($m = 5/8, n = 19/16$). The mean erosion rate is 0.5 km/Ma in the observed precipitation and effective mean precipitation scenarios and lower than 0.5 km/Ma in the observed mean precipitation and background precipitation scenarios. For each combination of m and n , the value of k is determined for the observed precipitation scenario, such that the mean erosion rate is 0.5 km/Ma and is kept the same for the other precipitation scenarios. For the m, n values of $(1/3, 2/3)$, $(1/2, 1)$, and $(5/8, 19/16)$, the values of k are 1.22×10^{-5} , 1.73×10^{-6} , and 3.15×10^{-7} , respectively, where the units of k are $\text{m}^{1-3m} \text{ yr}^{m-1}$. Triangle denotes the location of Mount Olympus.

precipitation rate required to erode at a certain rate is greater than the observed mean precipitation rate.

[54] In Figure 10, we show the predicted erosion rate patterns for three different fluvial erosion laws with m/n values near 0.5 : the unit shear stress model ($m = 1/3, n = 2/3$), the unit stream power model ($m = 1/2, n = 1$) and the model of Finnegan *et al.* [2004] ($m = 5/8, n = 19/16$). For each combination of m and n there are four predictions of the erosion rate pattern, one for each precipitation scenario (the observed precipitation pattern and uniform precipitation rates of p_{bg} , \bar{p} , and p^*). As expected, all predicted erosion rates increase from the coast toward Mount Olympus.

[55] At the broadest scale, the effect of the topography of the Olympic Mountains on precipitation is to increase the mean precipitation rate from a background precipitation, here assumed to be p_{bg} , to the observed mean precipitation, \bar{p} . Predicted mean erosion rates for the background

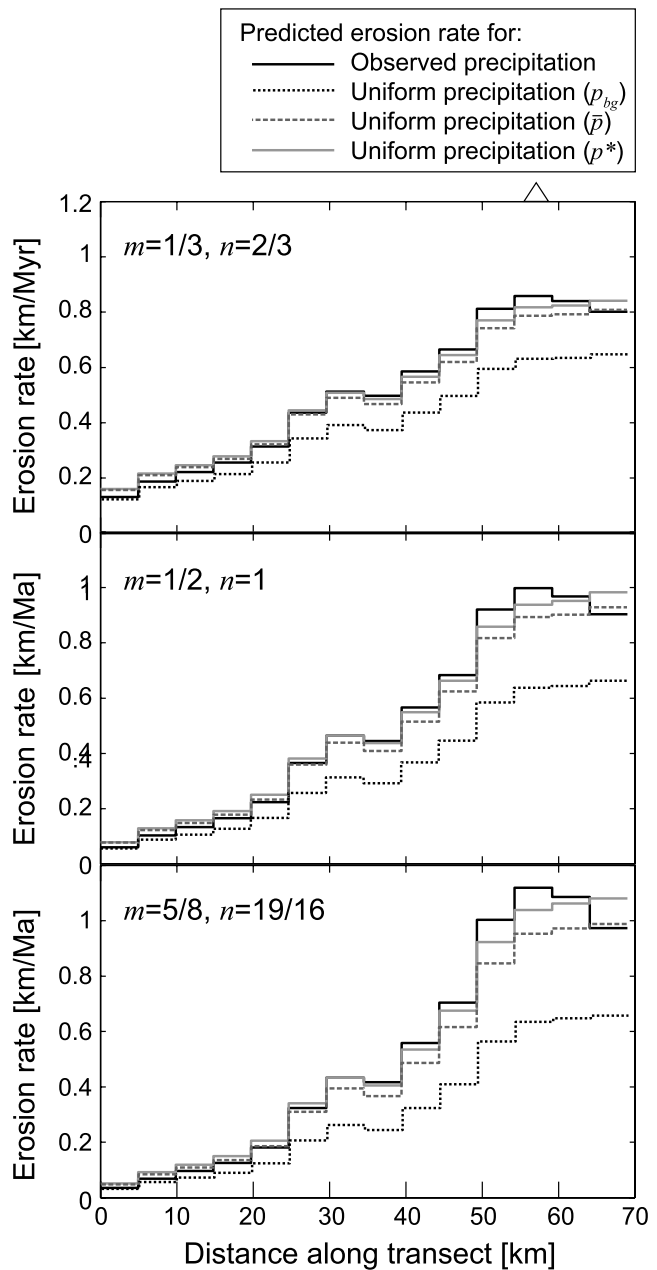


Table 1. Precipitation Forcing and Predicted Erosional Response at the Coast and Mount Olympus

Fluvial Erosion Law Exponents (Equation (1))	Coast		Mount Olympus	
	$m \frac{\Delta p}{p}, \%$	$\frac{\Delta e}{e}, \%$	$m \frac{\Delta p}{p}, \%$	$\frac{\Delta e}{e}, \%$
$m = 1/3, n = 2/3$	-14.6	-16.9	5.4	5.3
$m = 1/2, n = 1$	-22.6	-21.9	6.8	7.5
$m = 5/8, n = 19/16$	-28.6	-31.5	7.7	7.8

precipitation and observed mean precipitation scenarios are 0.31–0.39 km/Ma and 0.46–0.48 km/Ma, respectively. Thus the relative increase in mean erosion rate due to orographically enhanced precipitation is roughly 25–50%. A comparison of the mean erosion rates determined for the observed and effective mean precipitation scenarios (0.46–0.49 km/Ma and 0.5 km/Ma, respectively) suggests that the nonuniform weighting of precipitation on relief and erosion rate, described above, has a relatively small impact (<10%) on the erosion rate pattern.

[56] The influence of spatial variations in precipitation rate on the erosion rate pattern can be determined by comparing predictions from the observed precipitation and effective mean precipitation scenarios (black lines vs. light gray lines in Figure 10). Importantly, the differences in erosion rate between the two scenarios are proportionately small everywhere along the transect. Simply put, spatial variations in precipitation rate appear to have relatively little influence on the predicted erosion rate pattern. Thus we conclude that it is the amount, not the spatial variation, of orographic precipitation that has a significant influence on the erosion rate pattern in the Olympic Mountains. This result is entirely consistent with results from the numerical and trellis models; in those models, the large erosion rate response was caused by a 700% increase in precipitation rate, whereas in the case of the Olympic Mountains, the perturbations in precipitation and hence the predicted erosion rate responses are much smaller.

[57] Next, we compare predictions of the Olympic Mountains model with those of the trellis model to determine whether the simple principles derived from trellis model hold for a more realistic precipitation pattern and drainage network. We begin by noting that the erosion rate patterns for the observed precipitation and effective mean precipitation scenarios intersect where the observed mean precipitation profile (bold gray line in Figure 8c) is approximately equal to p^* (see plus signs in Figure 8c). For instance, near Mount Olympus, the observed precipitation rate is greater than the effective mean, and the erosion rate predicted for the observed precipitation scenario is greater than that predicted for the effective mean precipitation scenario. The opposite is true near the coast, where erosion rates are predicted to be higher in the effective mean precipitation scenario than in the observed precipitation scenario. These results match the results of previous sections: locally higher precipitation rates lead to locally higher erosion rates. Given this agreement, we can use the results in Figure 10 to quantitatively test whether the expressions derived from the trellis model (equations (12) and (B15)) are also valid for the Olympic Mountains.

[58] We define the difference between the observed precipitation rate, p , (bold gray line in Figure 8c) and the effective mean precipitation rate, p^* , at a point along the transect as

$$\frac{\Delta p}{p} = \frac{p - p^*}{p^*}, \quad (14)$$

and the difference in the erosion rate as

$$\frac{\Delta e}{e} = \frac{e - e^*}{e^*}, \quad (15)$$

where e is the erosion rate for the observed precipitation pattern and e^* is the erosion rate for the effective mean precipitation scenario. As defined by equations (14) and (15), there are negative perturbations in the precipitation and erosion rates near the coast and positive perturbations near Mount Olympus. In Table 1, we show the values of the precipitation forcing ($m\Delta p/p$) and the predicted erosional response ($\Delta e/e$) at the coast and at Mount Olympus for the three fluvial erosion laws considered thus far. In general, the erosional response is roughly equal to the precipitation forcing ($\Delta e/e \approx m\Delta p/p$), suggesting that the simple trellis model describes the Olympic Mountains reasonably well. From this agreement, we infer the differences in drainage network and precipitation pattern between the trellis model and the model of the Olympic Mountains have only a small effect on the predicted erosion rate pattern.

[59] Finally, we compare predictions from the model of the Olympic Mountains to two inferences of the long-term erosion rate pattern [Pazzaglia and Brandon, 2001; Stolar et al., manuscript in preparation, 2007] (Figure 11). The inferred curves have been determined from overlapping data sets: the western 35 km of the Pazzaglia and Brandon [2001] curve are mainly constrained by late Quaternary river incision rates; the eastern 35 km of the curve are constrained by apatite fission track (AFT) data; the Stolar et al. (manuscript in preparation, 2007) curve is constrained by many of the same AFT data, as well as zircon fission track data and apatite (U-Th)/He data. Note that the Stolar et al. (manuscript in preparation, 2007) curve is a smoothed regression of erosion rates determined from separate inversions of the three different thermochronometer data sets. For the predictions, we show the range of erosion rates for the observed precipitation pattern and the same three combinations of m and n presented in Figure 10. Two sets of predictions, each with a different mean erosion rate, are shown to allow comparison with the inferred erosion rate patterns.

[60] As shown in Figure 11, the inferred erosion rate patterns strongly support the theoretical expectations developed in this study that erosion rates are lower near the coast and higher in the interior of the range. The most notable discrepancy between the inferred and predicted erosion rate patterns is in the location of the maximum erosion rate: the maximum erosion rate from Pazzaglia and Brandon [2001] is offset approximately 20 km to the west of the other maximum erosion rates. However, the geologic significance of this offset is debatable. Stolar et al. (manuscript in preparation, 2007) have argued that the thermochronometer data available on the western side of the Olympics are not

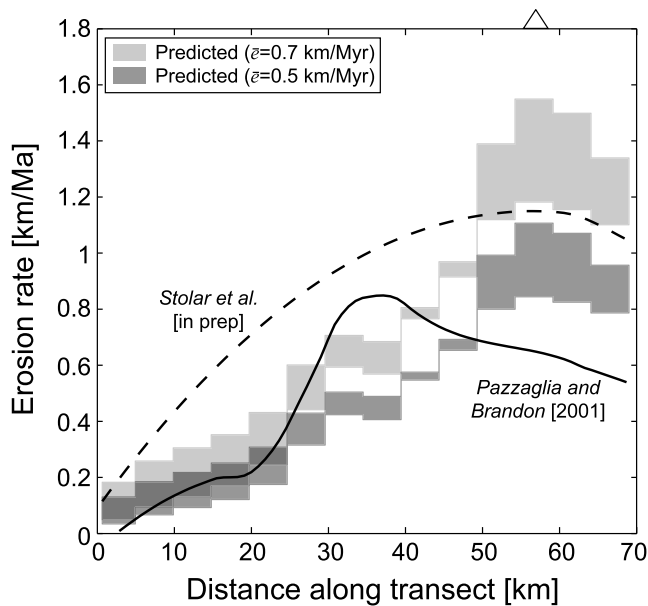


Figure 11. Comparison of inferred and predicted erosion rate patterns. Inferred erosion rate patterns are from Pazzaglia and Brandon [2001] (solid black line) and Stolar et al. (manuscript in preparation, 2007) (dashed black line). Range of erosion rates shown for $m, n = (1/3, 2/3), (1/2, 1),$ and $(5/8, 19/16)$ and for $\bar{z} = 0.5 \text{ km/Ma}$ (dark gray shading) and $\bar{z} = 0.7 \text{ km/Ma}$ (light gray shading) to allow comparison with the inferred curves. Inferred profiles were projected from their original orientation onto the transect shown in Figure 8. Triangle denotes the location of Mount Olympus.

sufficient to resolve a local maximum in erosion rate at 35 km and that the data only resolve a broad increase in erosion rate from the coast to Mount Olympus. Furthermore, the lack of detailed agreement is not surprising given the host of assumptions and uncertainties behind the inferred and predicted erosion rate patterns. Whether the disagreement is real or the reasons are knowable are topics that merit future scrutiny.

8. Discussion

[61] We first discuss the main results of our work and consider the generality of the underlying assumptions. Second, we compare results from different model frameworks to understand the length scales of the responses to nonuniform precipitation. Third, we argue that our results can be extended to some time-dependent scenarios.

8.1. Response to Uniform Precipitation

[62] Our results suggest that the rock uplift and erosion rate patterns in a critical orogen should be nonuniform even when forced by uniform precipitation. This is a natural consequence of linking an increasing critical topographic form with a branching drainage network: maintenance of the critical topographic form requires a nonuniform pattern of ridge-valley relief and hence a nonuniform pattern of rock uplift rate.

[63] The most important assumptions underlying this result are: (1) the critical topographic form increases from

the toe toward the divide and (2) the relationship between ridge-valley relief and rock uplift rate is positive and relatively constant across the orogen. Settings in which the first assumption is violated are likely to be characterized by local deposition, not erosion, [e.g., Fuller et al., 2005] and are therefore not relevant to this study.

[64] The second assumption seems appropriate for non-glaciated landscapes, as many fluvial and hillslope erosion laws predict a positive slope-rock uplift rate relationship at or near topographic steady state [e.g., Whipple and Tucker, 1999; Tucker and Whipple, 2002; Tucker, 2004; Gasparini et al., 2006; Roering et al., 2001]. Recent work on modeling erosion by debris flows [Stock and Dietrich, 2006] suggests a positive relationship between channel slope and erosion rate and hence rock uplift rate. Even in glaciated landscapes, only a very efficient “glacial buzz saw” would be capable of fundamentally changing the relief-rock uplift rate relationship [e.g., Brozovic et al., 1997; Mitchell and Montgomery, 2006]. It is possible that the drainage network might be configured such that generation of ridge-valley relief (and rock uplift rate) is favored near the toe relative to near the divide. However, given the general agreement between the results of the trellis model and the analysis of the Olympic Mountains (see Table 1), we do not expect that details of the drainage network, such as sinuosity and nonperpendicular tributary junctions, are a major control on the erosion rate pattern.

[65] It is also possible that the spatial pattern of substrate erodibility could be an important control on the erosion rate pattern. Stock and Montgomery [1999] demonstrated that k varies between different lithologies by several orders of magnitude. The results of Dadson et al. [2003] suggest that significant variations in k can influence the orogen-scale pattern of erosion. They showed that short-term erosion rates in Taiwan are extremely high where poorly consolidated foreland sediments are being deformed. In the case of the Olympic Mountains, if the rocks near the coast are much more easily eroded than rocks near Mount Olympus, it is conceivable that the erosion rate is uniform across the range or, perhaps, that the erosion rate decreases toward Mount Olympus. The available inferences of the erosion rate pattern would suggest otherwise, but the influence of erodibility on the erosion rate pattern is an intriguing possibility, and further work is needed to constrain how bedrock erodibility varies within individual orogens.

8.2. Response to the Box Car Pattern of Precipitation

[66] In the models presented here, the box car pattern of precipitation generates a weak topographic response and much stronger deformation and erosion rate responses. This follows from a large difference in the sensitivities of the main channel and ridge-valley relief to changes in the local precipitation rate. Because the critical topographic form requires that changes in the main channel elevation and ridge-valley relief be of similar magnitude and opposite sign ($\Delta z = -\Delta r/2$), a large change in rock uplift rate is required to offset a change in the local precipitation rate. In other words, the response of the tectonic-erosional system is a compromise between the topography, which has a tendency to lower, and the critical topographic form, which does not allow the mean elevation to change.

[67] These results rest primarily on the assumption that the stream power law describes erosion within the channel network. Importantly, the stream power law limits the channel response to one degree of freedom, the channel slope. Allowing for additional degrees of freedom (e.g., channel width and sediment cover) would presumably decrease the sensitivity of both the main channel elevation and ridge-valley relief to changes in precipitation; that is, the relief and rock uplift responses would be damped.

[68] Consideration of sediment cover [e.g., *Sklar and Dietrich*, 2004; *Gasparini et al.*, 2006], for instance, might also change the sign of the slope response to a change in precipitation. Depending on spatial variations in sediment discharge and capacity, it is conceivable that an increase in precipitation might lead to (1) an increase in erosion potential in main channel and a decrease in the tributary or (2) a decrease in erosion potential in the main channel and an increase in the tributary. In either case, this would lead to important differences in the tectonic and erosional response.

8.3. Length Scale of the Response to Nonuniform Precipitation

[69] In natural settings, the response to nonuniform precipitation should depend on length scales inherent to the climatic and tectonic systems. As one may have expected, the trellis and numerical models give different predictions, with the difference being due to how deformation is described in the two models. In the trellis model, the scale of the rock uplift response is set by the tributary basin width (see Figure 6b). This is a consequence of requiring that the linear mean elevation profile be maintained without specifying the operant tectonic processes (i.e., there is no length scale inherent to the tectonic system).

[70] The numerical model contains a more realistic description of brittle deformation, which imposes a minimum length scale to the tectonic response. As shown in Figures 2c and 2d, deformation is characterized by sets of conjugate shear zones that meet along the basal detachment. In a homogeneous, plastic material, the distance between these shear zones is determined by the crustal thickness and the orientation of the shear zones. This is illustrated in Figure 3c, which shows that the erosionally induced increases in deformation and erosion rate occur within a region that is bounded by two shear zones. Importantly, the width of this region is greater than the width of the zone of increased precipitation. Thus the minimum length scale of the response is set by the tectonic system. Because the tectonic model does not allow for description of faults with history-dependent material strengths, we cannot casually extend this result to natural settings. However, we expect natural structures, which represent persistent and significant mechanical heterogeneities, to have a strong influence on the scale and magnitude of the tectonic response to climatic forcing.

8.4. Time Dependence of the Erosion Rate Pattern

[71] Though we have limited our analyses to steady state orogens, our results should also be applicable to some transient systems. For instance, with the one-dimensional model presented in section 3, it is very simple to make the connection between the steady state and transient cases. Equation (3)

states a relationship between the erosion rate and the slope of the critical topographic form ($\tan \alpha$). This relationship follows directly from the stream power erosion law (equation (1)) and does not require an assumption of topographic steady state. Thus, regardless of whether the wedge grows self-similarly ($d\alpha/dt = 0$) or nonself-similarly, the erosion rate pattern should always be given by equation (3).

[72] A similar result can be argued for in more realistic tectonic-erosional systems. The mean topography of the numerical orogen grows self-similarly during much of the approach to steady state [*Stolar et al.*, 2006]. The numerical orogen also obeys the width-scaling law of *Whipple and Meade* [2004] and *Roe et al.* [2006]. *Roe et al.* [2006] demonstrated that the width-scaling law requires that the erosion rate pattern changes self-similarly as the wedge changes in size. This implies that the time-dependent erosion rate pattern must look like the steady state pattern. Note that this does not preclude self-similar growth of topography, which only requires a uniform surface uplift rate pattern, i.e., that rock uplift and erosion rates are different by the same amount over the orogen. Thus it is consistent that the time-dependent system exhibit self-similar mean topography, uniform surface uplift rate, and nonuniform rock uplift and erosion rates. Though this simple example demonstrates a possible outcome of an evolving orogen, the diversity of transient orogens clearly deserves more attention in the future.

9. Conclusions

[73] Our results indicate that topography plays a crucial role in the coupling between tectonics and erosion. This is most evident in the differences between the predictions of the trellis and one-dimensional models. In the one-dimensional model, the landscape is not allowed to depart from the critical topographic form. This constraint on the topography is easily translated to a constraint on the patterns of erosion and rock uplift rate, which are very different than those predicted by the trellis and numerical models. In the latter two models, the generation of ridge-valley relief has important consequences for the predicted patterns of erosion rate and deformation: maintenance of an increasing critical topographic form requires similar patterns of both ridge-valley relief and rock uplift rate. Thus spatial variations in erosion rate do not necessarily imply forcing from climate; this has important implications for interpreting spatial correlations between topography, precipitation and exhumation.

[74] Topography is also key to understanding the response of the tectonic-erosional system to spatial variations in precipitation. When perturbed by a local increase in precipitation, the system maintains the critical topographic form through a local increase in rock uplift rate, which greatly dampens the response of the ridge-valley relief. As applied to the western side of the Olympic Mountains, our model appears to explain the planform and mean topography and predicts that the spatial variation in precipitation has only a small effect on the predicted pattern of erosion rate.

Appendix A

[75] The landscape of the trellis model is composed of N pairs of matching tributary basins (Figure 4a). The across-

strike width of individual tributary basins, W_x^{trib} , is assumed to be equal to W_x^{trib*} , with the exception of the basin nearest the toe which, to fill space, has a width between $\frac{1}{2}W_x^{trib*}$ and $\frac{3}{2}W_x^{trib*}$. For the results presented here, the along-strike width of the model domain, W_y , scales linearly with the length of the wedge, W_x , which is suggested by natural basins [e.g., *Hovius*, 1996]. Holding W_y constant or changing the dependency on W_x does not affect the general results of this analysis.

[76] The elevation of the main channel at the junction with the i th tributary can be written as a finite sum:

$$z_i = s_i W_{xi}^{trib} / 2 + \sum_{j=i+1}^N s_j W_{xj}^{trib}, \quad (A1)$$

where i is an integer between one at the divide and N at the toe and s_i is the main channel slope. Equation (A1) can be rewritten using the stream power law (equation (1)) to express the channel slope:

$$z_i = \left(\frac{u_i}{k}\right)^{1/n} q_i^{-m/n} W_{xi}^{trib} / 2 + \sum_{j=i+1}^N \left(\frac{u_j}{k}\right)^{1/n} q_j^{-m/n} W_{xj}^{trib}. \quad (A2)$$

The discharge in the main channel is

$$q_i = \sum_{j=1}^i p_j W_{xj}^{trib} W_y. \quad (A3)$$

Because the rock uplift and precipitation rates are constant within individual tributary basins, the ridge-valley relief can be written as

$$r_i = s_c y_c + \int_{y_c}^{W_y/2} \left(\frac{u_i}{k}\right)^{1/n} q_i(y)^{-m/n} dy, \quad (A4)$$

where y is the distance from the tributary divide in the along-strike direction ($0 \leq y \leq W_y/2$), y_c is the position of the tributary channel head, the first term on the right-hand side is the hillslope component of the ridge-valley relief, the second term is the fluvial component of the ridge-valley relief, and the water discharge in the tributary is

$$q_i(y) = p_i W_{xi}^{trib} y.$$

Equation (A2) and equation (A4) can be substituted into a modified form of equation (4):

$$\bar{z}_i - (z_i + r_i/2) = 0, \quad (A5)$$

which can be solved using the Newton-Raphson method.

Appendix B

[77] We impose a perturbation of Δp on the precipitation rate within a single tributary basin. The linear approxima-

tions of the responses of the main channel elevation and ridge-valley relief are

$$\Delta z = \frac{\partial z}{\partial q} \Delta q + \frac{\partial z}{\partial u} \Delta u \quad (B1)$$

and

$$\Delta r = \frac{\partial r}{\partial p} \Delta p + \frac{\partial r}{\partial u} \Delta u. \quad (B2)$$

For the mean elevation to be maintained, the changes in main channel elevation and ridge-valley relief must be related by

$$\Delta z = -\Delta r/2. \quad (B3)$$

[78] The change in main channel elevation is related to the change in main channel slope, Δs , by

$$\Delta z = \Delta s \frac{W_x^{trib}}{2}, \quad (B4)$$

and equation (B1) can be rewritten in terms of changes in the main channel slope:

$$\Delta z = \frac{W_x^{trib}}{2} \left(\frac{\partial s}{\partial u} \Delta u + \frac{\partial s}{\partial q} \Delta q \right). \quad (B5)$$

Rearranging equation (1) and differentiating gives

$$\frac{\partial s}{\partial u} = \frac{1}{n} \frac{1}{u} s \quad (B6)$$

and

$$\frac{\partial s}{\partial q} = -\frac{m}{n} \frac{1}{q} s. \quad (B7)$$

Substituting these into equation (B1) yields

$$\Delta z = \frac{1}{n} s \frac{W_x^{trib}}{2} \left(\frac{\Delta u}{u} - m \frac{\Delta q}{q} \right). \quad (B8)$$

[79] The ridge-valley relief, r , is the sum of the fluvial and hillslope relief within a tributary basin. The relief on a threshold hillslope, r_h , is

$$r_h = \left(\frac{u}{k}\right)^{\frac{1}{n}} (W_x^{trib} p)^{-1} s_c^{1-\frac{n}{m}}. \quad (B9)$$

For $m = n$, the fluvial relief, r_f , is

$$r_f = \left(\frac{u}{k}\right)^{\frac{1}{n}} (W_x^{trib} p)^{-1} \left(\ln\left(\frac{W_y}{2}\right) - \frac{1}{m} \ln\left(\frac{u}{k}\right) + \ln(p W_x^{trib} s_c) \right), \quad (B10a)$$

and, for $m \neq n$, it is

$$r_f = \left(\frac{n}{n-m}\right) \left(\left(\frac{u}{k}\right)^{\frac{1}{n}} (W_x^{\text{trib}} p)^{-\frac{m}{n}} \left(\frac{W_y}{2}\right)^{1-\frac{m}{n}} - \left(\frac{u}{k}\right)^{\frac{1}{m}} (W_x^{\text{trib}} p)^{-1} s_c^{1-\frac{m}{m}}\right). \quad (\text{B10b})$$

The derivatives of ridge-valley relief with respect to rock uplift rate and precipitation rate—after some algebra—can be written as

$$\frac{\partial r}{\partial u} = \frac{1}{nu} r_f \quad (\text{B11})$$

and

$$\frac{\partial r}{\partial p} = -\frac{m}{n} r_f. \quad (\text{B12})$$

Substituting these into equation (B2) yields the net change in ridge-valley relief:

$$\Delta r = \frac{1}{n} r_f \left(\frac{\Delta u}{u} - m \frac{\Delta p}{p}\right). \quad (\text{B13})$$

For an increase in precipitation rate within a tributary, the constraints are $0 \leq \Delta q/q \leq \Delta p/p$, and $\Delta z = -\Delta r/2$, and equations (B8) and (B13) reduce to

$$m \frac{\Delta q}{q} \leq \frac{\Delta u}{u} \leq m \frac{\Delta p}{p}. \quad (\text{B14})$$

For a decrease in precipitation rate (i.e., $\Delta p/p \leq \Delta q/q \leq 0$), the inequality is

$$m \frac{\Delta p}{p} \leq \frac{\Delta u}{u} \leq m \frac{\Delta q}{q}. \quad (\text{B15})$$

Notation

e	erosion rate, m yr ⁻¹ .
H	thickness of incoming crust, m.
h	distance exponent in Hack's law.
k	coefficient of fluvial erosion, m ^{1-3m} yr ^{1-m} .
k_a	coefficient in Hack's law, m ^{2-h} .
m	discharge exponent in stream power law.
n	slope exponent in stream power law.
p	precipitation rate, m yr ⁻¹ .
q	water discharge, m ³ yr ⁻¹ .
r	ridge-valley relief, m.
r_f	fluvial relief, m.
r_h	hillslope relief, m.
s	channel slope.
s_c	hillslope gradient.
u	vertical rock velocity, m yr ⁻¹ .
v	horizontal rock velocity, m yr ⁻¹ .
v_c	convergence velocity, m yr ⁻¹ .
W_x	across-strike width of trellis landscape, m.
W_x^{trib}	across-strike width of a tributary, m.
$W_x^{\text{trib}*}$	standard across-strike width of a tributary, m.
W_y	along-strike width of trellis landscape, m.

x	across-strike coordinate, m.
y	along-strike coordinate, m.
y_c	location of tributary channel head, m.
z	vertical coordinate and main channel elevation, m.
\bar{z}	mean elevation, m.
α	mean slope of the wedge.
γ_r	sensitivity factor for relief change, m.
γ_z	sensitivity factor for main channel change, m.

[80] **Acknowledgments.** We thank Jean-Phillipe Avouac, Edward Sobel, and the associate editor for constructive reviews and Alison Anders and Cliff Mass for providing the precipitation data for the Olympic Mountains. G. H. Roe and D. B. Stolar received support from the National Science Foundation Continental Dynamics Program (EAR-6312293).

References

- Anders, A. M., G. H. Roe, D. R. Durran, and J. R. Minder (2007), Small-scale spatial gradients in climatological precipitation on the Olympic Peninsula, *J. Hydrometeorol.*, in press.
- Avouac, J. P., and E. B. Burov (1996), Erosion as a driving mechanism of intracontinental mountain growth, *J. Geophys. Res.*, *101*, 17,747–17,770.
- Batt, G. E., M. T. Brandon, K. A. Farley, and M. Roden-Tice (2001), Tectonic synthesis of the Olympic Mountains segment of the Cascadia wedge, using two-dimensional thermal and kinematic modeling of thermochronological ages, *J. Geophys. Res.*, *106*, 26,731–26,746.
- Beaumont, C., P. Fullsack, and J. Hamilton (1992), Erosional control of active compressional orogens, in *Thrust Tectonics*, edited by K. McClay, pp. 19–31, Chapman and Hall, New York.
- Beaumont, C., P. J. J. Kamp, J. Hamilton, and P. Fullsack (1996), The continental collision zone, South Island, New Zealand: Comparison of geodynamical models and observations, *J. Geophys. Res.*, *101*, 3333–3360.
- Beaumont, C., R. A. Jamieson, M. H. Nguyen, and B. Lee (2001), Himalayan tectonics explained by extrusion of a low-viscosity crustal channel coupled to focused surface denudation, *Nature*, *414*(6865), 738–742.
- Brandon, M. T., and A. R. Calderwood (1990), High-pressure metamorphism and uplift of the Olympic subduction complex, *Geology*, *18*, 1252–1255.
- Brandon, M. T., M. K. Roden-Tice, and J. I. Garver (1998), Late Cenozoic exhumation of the Cascadia accretionary wedge in the Olympic Mountains, northwest Washington State, *Geol. Soc. Am. Bull.*, *110*, 985–1009.
- Braun, J., and M. Sambridge (1997), Modelling landscape evolution on geological time scales: A new method based on irregular spatial discretization, *Basin Res.*, *9*(1), 27–52.
- Brozovic, N., D. W. Burbank, and A. J. Meigs (1997), Climatic limits on landscape development in the northwestern Himalaya, *Science*, *276*(5312), 571–574.
- Dadson, S. J., et al. (2003), Links between erosion, runoff variability and seismicity in the Taiwan orogen, *Nature*, *426*(6967), 648–651.
- Dahlen, F. A. (1984), Noncohesive critical Coulomb wedges: An exact solution, *J. Geophys. Res.*, *89*, 125–133.
- Davis, D., J. Suppe, and F. A. Dahlen (1983), Mechanics of fold-and-thrust belts and accretionary wedges, *J. Geophys. Res.*, *88*, 1153–1172.
- Finnegan, N., G. H. Roe, D. R. Montgomery, and B. Hallet (2004), A scaling relationship for channel width in bedrock rivers, *Geology*, *33*, 229–232.
- Fuller, C. W., S. D. Willett, and M. T. Brandon (2005), Formation of forearc basins and their influence on subduction zone earthquakes, *Geology*, *34*, 65–68.
- Gasparini, N. M., R. L. Bras, and K. X. Whipple (2006), Numerical modeling of non-steady-state river profile evolution using a sediment-flux-dependent incision model, in *Tectonics, Climate, and Landscape Evolution*, edited by S. D. Willett et al., *Penrose Conf. Ser., Spec. Pap. Geol. Soc. Am.*, 398, 127–142.
- Godard, V., R. Cattin, and J. Lavé (2004), Numerical modeling of mountain building: Interplay between erosion law and crustal rheology, *Geophys. Res. Lett.*, *31*, L23607, doi:10.1029/2004GL021006.
- Hilley, G. E., and M. R. Strecker (2004), Steady state erosion of critical Coulomb wedges with applications to Taiwan and the Himalaya, *J. Geophys. Res.*, *109*, B01411, doi:10.1029/2002JB002284.
- Hilley, G. E., M. R. Strecker, and V. A. Ramos (2004), Growth and erosion of fold-and-thrust belts with an application to the Aconcagua fold-and-thrust belt, Argentina, *J. Geophys. Res.*, *109*, B01410, doi:10.1029/2002JB002282.
- Hovius, N. (1996), Regular spacing of drainage outlets from linear mountain belts, *Basin Res.*, *8*(1), 29–44.

- Lavé, J. (2005), Analytic solution of the mean elevation of a watershed dominated by fluvial incision and hillslope landslides, *Geophys. Res. Lett.*, *32*, L11403, doi:10.1029/2005GL022482.
- Lavé, J., and J. P. Avouac (2001), Fluvial incision and tectonic uplift across the Himalayas of central Nepal, *J. Geophys. Res.*, *106*, 26,561–26,592.
- McCaffrey, R., M. D. Long, C. Goldfinger, P. C. Zwick, J. L. Nabelek, C. K. Johnson, and C. Smith (2000), Rotation and plate locking at the southern Cascadia subduction zone, *Geophys. Res. Lett.*, *27*, 3117–3120.
- Miller, M. M., D. J. Johnson, C. M. Rubin, H. Dragert, K. Wang, A. Qamar, and C. Goldfinger (2001), GPS-determination of along-strike variation in Cascadia margin kinematics: Implications for relative plate motion, subduction zone coupling, and permanent deformation, *Tectonics*, *20*(2), 161–175.
- Mitchell, S. G., and D. R. Montgomery (2006), Influence of a glacial buzz-saw on the height and morphology of the Cascade Range in central Washington state, USA, *Quat. Res.*, *65*, 96–107.
- Montgomery, D. R. (2001), Slope distributions, threshold hillslopes, and steady-state topography, *Am. J. Sci.*, *301*, 432–454.
- Montgomery, D. R. (2002), Valley formation by fluvial and glacial erosion, *Geology*, *30*, 1047–1050.
- Montgomery, D. R., and M. T. Brandon (2002), Topographic controls on erosion rates in tectonically active mountain ranges, *Earth Planet. Sci. Lett.*, *201*(3–4), 481–489.
- Montgomery, D. R., and H. M. Greenberg (2000), Local relief and the height of Mount Olympus, *Earth Surf. Processes Landforms*, *25*(4), 385–396.
- Pazzaglia, F. J., and M. T. Brandon (2001), A fluvial record of long-term steady-state uplift and erosion across the Cascadia forearc high, western Washington State, *Am. J. Sci.*, *301*, 385–431.
- Roe, G. H. (2005), Orographic precipitation, *Annu. Rev. Earth Planet. Sci.*, *33*, 645–671.
- Roe, G. H., D. R. Montgomery, and B. Hallet (2003), Orographic precipitation and the relief of mountain ranges, *J. Geophys. Res.*, *108*(B6), 2315, doi:10.1029/2001JB001521.
- Roe, G. H., D. B. Stolar, and S. D. Willett (2006), Response of a steady-state critical wedge orogen to changes in climate and tectonic forcing, in *Tectonics, Climate, and Landscape Evolution*, edited by S. D. Willett et al., *Penrose Conf. Ser., Spec. Pap. Geol. Soc. Am.*, 398, 227–239.
- Roering, J. J., J. W. Kirchner, L. S. Sklar, and W. E. Dietrich (2001), Hillslope evolution by nonlinear creep and landsliding: An experimental study, *Geology*, *29*, 143–146.
- Sklar, L. S., and W. E. Dietrich (2001), Sediment and rock strength controls on river incision into bedrock, *Geology*, *29*, 1087–1090.
- Sklar, L. S., and W. E. Dietrich (2004), A mechanistic model for river incision into bedrock by saltating bed load, *Water Resour. Res.*, *40*, W06301, doi:10.1029/2003WR002496.
- Snyder, N. P., K. X. Whipple, G. E. Tucker, and D. J. Merritts (2003), Importance of a stochastic distribution of floods and erosion thresholds in the bedrock river incision problem, *J. Geophys. Res.*, *108*(B2), 2117, doi:10.1029/2001JB001655.
- Stock, J. D., and W. E. Dietrich (2006), Erosion of steepland valleys by debris flows, *Geol. Soc. Am. Bull.*, *118*, 1125–1148.
- Stock, J. D., and D. R. Montgomery (1999), Geologic constraints on bedrock river incision using the stream power law, *J. Geophys. Res.*, *104*, 4983–4993.
- Stolar, D. B., S. D. Willett, and G. H. Roe (2006), Climatic and tectonic forcing of a critical orogen, in *Tectonics, Climate, and Landscape Evolution*, edited by S. D. Willett et al., *Penrose Conf. Ser., Spec. Pap. Geol. Soc. Am.*, 398, 241–250.
- Tabor, R. W., and W. H. Cady (1978), Geologic map of the Olympic Peninsula, *U.S. Geol. Surv. Map*, I-994.
- Tucker, G. E. (2004), Drainage basin sensitivity to tectonic and climatic forcing: Implications of a stochastic model for the role of entrainment and erosion thresholds, *Earth Surf. Processes Landforms*, *29*(2), 185–205.
- Tucker, G. E., and K. X. Whipple (2002), Topographic outcomes predicted by stream erosion models: Sensitivity analysis and intermodel comparison, *J. Geophys. Res.*, *107*(B9), 2179, doi:10.1029/2001JB000162.
- Wang, W. H., and D. M. Davis (1996), Sandbox model simulation of forearc evolution and noncritical wedges, *J. Geophys. Res.*, *101*, 11,329–11,339.
- Wang, K., R. Wells, S. Mazzotti, R. D. Hyndman, and T. Sagiya (2003), A revised dislocation model of interseismic deformation of the Cascadia subduction zone, *J. Geophys. Res.*, *108*(B1), 2026, doi:10.1029/2001JB001227.
- Wells, R. E. (1990), Paleomagnetic rotations and the Cenozoic tectonics of the Cascade Arc, Washington, Oregon, and California, *J. Geophys. Res.*, *95*, 19,409–19,417.
- Whipple, K. X., and B. J. Meade (2004), Controls on the strength of coupling among climate, erosion, and deformation in two-sided, frictional orogenic wedges at steady state, *J. Geophys. Res.*, *109*, F01011, doi:10.1029/2003JF000019.
- Whipple, K. X., and B. J. Meade (2006), Orogen response to changes in climatic and tectonic forcing, *Earth Planet. Sci. Lett.*, *243*, 218–228.
- Whipple, K. X., and G. E. Tucker (1999), Dynamics of the stream-power river incision model: Implications for height limits of mountain ranges, landscape response timescales, and research needs, *J. Geophys. Res.*, *104*, 17,661–17,674.
- Whipple, K. X., and G. E. Tucker (2002), Implications of sediment-flux-dependent river incision models for landscape evolution, *J. Geophys. Res.*, *107*(B2), 2039, doi:10.1029/2000JB000044.
- Whipple, K. X., E. Kirby, and S. H. Brocklehurst (1999), Geomorphic limits to climate-induced increases in topographic relief, *Nature*, *401*(6748), 39–43.
- Whipple, K. X., G. S. Hancock, and R. S. Anderson (2000), River incision into bedrock: Mechanics and relative efficacy of plucking, abrasion, and cavitation, *Geol. Soc. Am. Bull.*, *112*, 490–503.
- Willett, S. D. (1999a), Orogeny and orography: The effects of erosion on the structure of mountain belts, *J. Geophys. Res.*, *104*, 28,957–28,981.
- Willett, S. D. (1999b), Rheological dependence of extension in wedge models of convergent orogens, *Tectonophysics*, *305*(4), 419–435.
- Willett, S., C. Beaumont, and P. Fullsack (1993), Mechanical model for the tectonics of doubly vergent compressional orogens, *Geology*, *21*, 371–374.

G. Roe, Department of Earth and Space Sciences, University of Washington, Box 351310, Seattle, WA 98195, USA.

D. Stolar, School of Earth and Space Exploration, Arizona State University, Box 871404, Tempe, AZ 85287, USA. (dstolar@asu.edu)

S. Willett, Geologisches Institut, Eidgenössische Technische Hochschule, CH-8092 Zürich, Switzerland.